

A soft robot for peripheral lung cancer diagnosis and therapy

Max McCandless^{1,†}, Alexander Perry^{1,†}, Nicholas DiFilippo¹,
Ashlyn Carroll¹, Ehab Billatos², Sheila Russo^{1,3 *}

¹Mechanical Engineering Department, Boston University

²Medical School, Boston University

³Materials Science and Engineering Division, Boston University

Keywords: Surgical Robotics, Soft Robotics, Soft Actuators, Lung Cancer, Computer Vision.

*To whom correspondence should be addressed; E-mail: russos@bu.edu.

[†]Indicates shared first authorship.

Lung cancer is one of the deadliest forms of cancers and is often diagnosed by performing biopsies with the use of a bronchoscope. However, this diagnostic procedure is limited in ability to explore deep into the periphery of the lung where cancer can remain undetected. In this paper, we present design, modeling, fabrication, and testing of a one degree of freedom soft robot with integrated diagnostic and interventional capabilities as well as vision sensing. The robot can be deployed through the working channel of commercial bronchoscopes or used as a standalone system as it integrates a micro camera to provide vision sensing and controls to the periphery of the lung. The small diameter (2.4 mm) of the device allows navigation in branches deeper in the lung, where current devices have limited reachability. We have performed mechan-

ical characterizations of the robotic platform, including blocked force, maximum bending angle, maximum angular velocity, and workspace, and assessed its performance in *in-vitro* and *ex-vivo* experiments. We have developed a computer vision algorithm, and validated it in *in-vitro* conditions, to autonomously align the robot to a selected branch of the lung and aid the clinician (by means of a graphic user interface) during navigation tasks, and to perform robotic-assisted stabilization in front of a lesion, with automated tracking and alignment.

1 Introduction

Among all types of cancers, lung cancer has the highest death rate. Of the 228,820 new cases of lung cancer estimated to be diagnosed in 2020, an estimated 135,720 are expected to result in deaths (1). This is due, in part, to the frequent failure to detect lung cancer at its earliest and potentially curable stage: less than 20% of lung cancer patients are diagnosed in their early stage (2). Therefore, early diagnosis and treatment is of paramount importance to increase the survival rate of lung cancer and can only be achieved via accurate tissue sampling (3). This can be particularly challenging in the work-up of peripheral indeterminate pulmonary nodules due to their deep location within the lung. Medical imaging is the first screening method to detect potentially malignant nodules, however biopsy is necessary for definitive diagnosis (4). Biopsies can be obtained percutaneously or bronchoscopically. The latter method is often preferred as it doesn't require puncturing the pleura that may cause complications, such as pneumothorax (*i.e.*, lung collapse) (5). Nevertheless, traditional bronchoscopes cannot access small bronchi and navigate easily through the peripheral lung because of their large diameter, typically around 5-6 mm (6, 7). In addition, current endoscopic tools have limited dexterity and sensor feedback, thus limiting not just diagnostic but also therapeutic capabilities, and the possibility of perform-

ing advanced surgical tasks at the site of intervention, such as targeted drug delivery. The main causes of this rely on the design of the endoscopic instrumentation itself. Traditional endoscopes are based on conventional cable-driven actuation, which is prone to friction, backlash, hysteresis, and wear after multiple uses, that can affect precision and accuracy (8). Performing diagnosis and delivering therapy through these platforms introduces several challenges in terms of instrument controllability, stability, and capability to provide accurate and repeatable dexterous motions at the surgical site (9).

Robotic platforms for interventional bronchoscopy and navigation systems have been developed to tackle these issues and are now available on the market. The Auris Health Inc. MonarchTM Platform is using flexible robotics and cable driven actuation to create a bronchoscope robot (composed of two independently controlled telescoping, articulating devices – a bronchoscope and an outer sheath) to ease navigation in the peripheral lung (10). This is achieved using a joystick interface to control the robot in a more intuitive way with respect to a traditional bronchoscope. However, the outer diameter (OD) of this system is still quite large (bronchoscope OD is 4.4 mm and outer sheath OD is 6 mm). The IonTM Endoluminal system from Intuitive Surgical consists of a 3.5 mm cable-driven robotic bronchoscope with one bending degree of freedom and an integrated vision probe, which needs to be removed to insert interventional tools (*i.e.*, needles) to perform biopsies (11). The Medtronic superDimensionTM Navigation System utilizes fluoroscopic navigation technology to guide a robot in hard-to-reach areas of the lung (12). Once the target area is within reach, the system requires removal of the navigation probe to insert interventional tools (similarly to the IonTM Endoluminal system), which need to be constantly switched in the working channel.

Substantial research efforts are currently ongoing to enable robotic access and surgery in deep locations of the body (13, 14), such as the bronchial tree and the trachea, and to improve image-based navigation methods in the lungs (15, 16). Recent research advances in robotic

catheters have shown encouraging results in improved accuracy and repeatability of tip position control (17, 18). The Virtuoso Surgical (Virtuoso Surgical Inc., Nashville, TN, USA) system has recently demonstrated treatment of central airway obstruction (19). So far, only a few research groups have proposed surgical robotic platforms for lung cancer surgery; however, these systems do not embed vision probes (20) nor interventional tools (21). Soft robotic systems are currently being investigated for minimally invasive surgical applications (22–26) and they represents a promising approach in the field of interventional bronchoscopy because soft robots are constructed from compliant materials, thus they are inherently safe (27), and can be manufactured at small-scale sizes (28–30). Mechanical performance of soft actuators for robotic applications at different scales are discussed in (31). Another advantage of soft surgical robots is distal soft fluidic actuation, which can ensure safe interaction with biological tissue even in case of failure and no loss due to friction or backlash (32, 33). A soft actuator with a 7 mm diameter and $\approx 60^\circ$ bending range was proposed for bronchoscopy in (34). The field is still in its infancy but growing rapidly and review papers on general biomedical applications of soft robotics, soft robotics in minimally invasive surgery, and soft robotics in endoscopy can be found in (33, 35–37).

In this paper, we present a 2.4 mm soft robot with integrated vision sensing as well as diagnostic and interventional capabilities (Fig. 1, also please refer to Movie S1). The system is actuated through a one degree of freedom (DOF) soft pneumatic micro chamber that provides full retroflexion (*i.e.*, bending backwards – 180°). It can be deployed through the working channel of a bronchoscope or be used as a stand-alone system as the vision probe does not need to be removed to insert interventional tools, thus avoiding the need to perform “blind” surgical tasks. The purpose of this miniaturized device is to address critical unmet needs within the world of lung cancer, such as increasing the depth of access in peripheral regions of the bronchial tree, improving navigability within the lungs, and facilitating rapid diagnosis and

simultaneous treatment of lung cancer.

2 Clinical Requirements

Clinical requirements for the soft robot were identified as a first step during the design and development phase.

The robot needs to be designed to be integrated with current endoscopic instrumentation without disrupting endoluminal navigation or surgical workflow, while avoiding the necessity for dedicated or customized instruments, thus making it easy and intuitive to use by the clinician and minimizing their learning curve. The typical internal diameter (ID) of bronchoscopes working channels ranges from 2.2 to 3.2 mm (6). The proposed system needs to be capable of accessing deeper locations in the peripheral lung with respect to traditional bronchoscopes, that typically have an OD ranging from 5 to 6.3 mm, thus getting in closer proximity to a lesion.

Current bronchoscopes have one bending degree of freedom and a camera. They are rotated manually from the clinician during the examination. Patients are fully sedated during bronchoscopy so that they do not feel the discomfort of having the tube down their mouth or in their nose. Because the robot needs to navigate in the bronchial tree complex anatomy, it needs to be equipped with similar distal dexterity and sensor feedback capabilities.

The need to remove vision or navigation probes presented by some commercial robotic bronchoscopes (See Section 1) can potentially decrease the accuracy and precision of these systems, as it can cause displacement of the tip away from the ideal position, with no way to compensate for this accidental movement, since the clinician is performing “blind” surgical tasks at this stage. To avoid this, the robot must maintain direct visual feedback and direct guidance during navigation to the peripheral lung throughout the duration of the procedure as well as location of the targeted lesion. This will also help minimizing risks of X-rays exposure (associated with traditional fluoroscopy or computed tomography) for the patient and the clinician.

Current systems also introduce a “delay in diagnosis” (38). The process of bringing a patient in for a procedure takes sometimes two to four weeks and if diagnosis is missed by a “blind biopsy” that captures healthy lung tissue rather than the actual tumor, it may take another month before a patient can get back into the operative room (*e.g.*, one week to get the biopsy results, one to two weeks to schedule them in clinic to follow-up on those results and tell them they need to try again, another two to four weeks to schedule, another week to get the results again). That’s if everything goes right and does not include patient frustration and potentially leaving to go elsewhere or getting lost to follow-up altogether (39, 40). Late diagnosis and therapy lower the chance of survival and increases health care costs, therefore it is crucial to develop a solution to get accurate results and treatment. The robot must provide the capability to puncture lung tissue to perform biopsies and drug delivery, at the surgical area of interest, through robotic-assisted tracking and stabilization in front of the lesion. The main goal of this requirement is to enhance precision and avoid performing inaccurate biopsies and generating false negatives as well as hampering precise and accurate drug delivery in a desired location. Since forces required to puncture lung tissue are not known in the literature, we performed *ex-vivo* tests to evaluate them and designed our system so that it could meet this specific clinical requirement (see Section 4.1). Two separate working ports need to be integrated to deliver, for the first time, simultaneous (*i.e.*, within the same bronchoscopy procedure) diagnostic and therapeutic capabilities in early stage lung cancer. This can potentially shorten delays in diagnosis and treatment of lung cancer. We envisage that this system will allow real time diagnosis and therapy, with the aid of digital microscopy techniques and on-site pathology (41–43). The development and use of chemotherapy drugs is not part of the scope of the paper. We instead focus on the design and integration of the delivery system. The drug will be simulated by dyed water that will be visually inspected to evaluate successful therapy delivery. Simultaneous diagnosis and therapy within a single bronchoscopy procedure can be a promising approach towards battling lung can-

cer: a few studies have shown that each week that a patient with a new diagnosis of early lung cancer awaits surgery significantly increases the risk for tumor growth, spread and “upstaging”. Specifically, patients with stage I non-small cell lung cancer have a 4% increased risk of upstaging generally (to stage II, III, or IV) each week until their surgery. Their risk of upstaging to stage III disease was 1.3% per week of surgery delay (44). The second working port has a dual function as it can also be used when visualization is hampered by bleeding (for instance, when a lesion of interest begins to bleed after the initial biopsy but more tissue is needed). The second port could be used to deliver saline solution to clean out the area and improve visualization.

3 Materials and Methods

This section describes the soft robot design, fabrication, image capture and control system, and surgical workflow. A schematic diagram is shown in Fig. S1.

3.1 Soft Robot Design

We propose a miniaturized, multi-functional soft robot (2.4 mm diameter) that can be deployed from the working channel of current bronchoscopes or be used as a standalone system to reach the peripheral lung and enhance current diagnostic and therapeutic capabilities in early stage lung cancer detection and treatment. The robot (Fig. 1) is composed of a soft body that provides safe interaction with the surrounding environment during navigation in the anatomy. The main body is designed to have four microchannels (Fig. 1, C) to integrate: 1) a one DOF soft actuation chamber, 2) two working channels for biopsy and drug delivery end-effectors, and 3) a micro camera. The one DOF soft actuation chamber is integrated to steer the robot tip and aid navigation in peripheral lung locations as well as assist in diagnosis and targeted therapy tasks by positioning end-effector tools in front of the target surgical area. An end-effector biopsy tool and an end-effector delivery tool (Fig. 1, D), each consisting of a microneedle attached to a

channel, are used to respectively aspirate biological material (for diagnostic purposes) and inject fluids into a lesion (*i.e.*, chemotherapy drugs), thus paving the way to simultaneous diagnosis and targeted therapy. A 1.2 mm diameter micro camera (microScout Cam 1.2, Medigus Ltd., Omer, Israel) shown in Fig. 1, D, selected for its small size, provides visual feedback and direct guidance during navigation to the peripheral lung throughout the duration of the procedure as well as location of the targeted lesion.

3.2 Soft Robot Fabrication

The soft robot was fabricated out of Dragon Skin 00-10 Medium (Smooth-On, USA) casted in a four-piece CNC machined aluminum mold (Fig. 1, F). The mold (Fig. 1, F) is composed of two pieces with a groove to shape the cylindrical body of the robot (*i.e.*, bottom and top parts), and two lateral parts (end caps) with holes to allow integration of metal pins to form four microchannels and produce the cross section shown in Fig. 1, C. The size and position of the pins necessary to meet the clinical requirements was informed through Finite Element Analysis (FEA) experiments. The dimensions of the pins are as follows: the micro camera channel pin is 1.24 mm, the working channels pins are 0.56 mm, and the actuation chamber channel pin is 0.36 mm. The mold end caps are interchangeable, which permits implementation of new robot designs without the need to re-fabricate the entire mold assembly.

The fabrication process (see Fig. 1, F and Movie S2) of the device began with assembling the mold base, lateral end caps, and masking pins (see Step 1 in Fig. 1, F). Then, the silicone polymer was mixed in a 1:1 ratio with the addition of 5-6% by-mass OS-2 solvent (Dow Corning, USA), poured over both components of the exposed mold cavity, then degassed in a chamber at a vacuum pressure of 100 kPa for 5 minutes (bottom component shown in Step 2 in Fig. 1, F). Finally, the top piece of the mold was mounted, displacing the excess polymer. The sealed cavity was then cured at 70° C for 45 minutes (Step 3 in Fig. 1, F). Once curing

was complete, the masking pins were removed and the device was removed from the cavity. The smallest (0.36 mm) channel is sealed at the end of the fabrication process by injecting a silicone plug in one end of the device and inserting a piece of tubing (Micro Renathane Tubing 0.254 mm, Braintree Scientific, USA) in the other end (via bonding a 25 G needle segment to the tubing and actuation chamber), to create an air-tight actuation chamber to provide the robot with one bending DOF (Fig. 1, B). Air is used as the actuation fluid and chamber pressurization is controlled by means of a syringe pump (Pump 11 Pico Plus Elite, Harvard Apparatus, USA) and is monitored by a pressure sensor (BSP B010-EV002-A00A0B-S4, Balluff Inc., USA) with data collection from an Arduino Mega 2560. The fabricated robot tip is mounted on a flexible plastic tubing (McMaster, USA), acting as the robot body (Fig. 1, E), and the micro camera as well as biopsy and delivery needles are inserted in the working channels (Fig. 1, D). The final system consists of a 2.4 mm diameter soft robot (Fig. 1, E). The larger (1.24 mm) working channel on the bottom of the device is designed to integrate the micro camera and the medium-sized (0.56 mm) working channels on the sides are designed to integrate biopsy and delivery needles. The needle tools consist of two 30 G (0.312 mm) diameter stainless steel needles, which were laser machined to create a sharp 75° profile cut. A refurbished commercial bronchoscope (EX-ERA II BF-1TQ180, Olympus, Japan), with a 6.3 mm OD and 2.8 mm working channel ID, was selected to test the platform (Fig. 1, B).

3.3 Image Capture and Control System

The image capture and control system consists of hardware and software components (Fig. S1) which enable vision, navigation, stabilization in front of a lesion, and operator input through a graphic user interface (GUI), and are explained in the following subsections.

3.3.1 System Hardware

The micro camera captures video images at a resolution of 220×224 pixels with a frame rate of 30 fps. The unedited video signal from the micro camera initially passes through a digital signal processor (DSP) video processor (Medigus Ltd., USA), which converts the video to an HDMI output. Still frames are captured via a USB capture device (USB Capture HDMI Gen. 2, Magewell, China) connected to a workstation running Ubuntu 16.04 LTS with 16 GB RAM. Each frame is converted to an OpenCV (OpenCV (C++), version 4.1.0) `Mat` `container` class, which enables further image processing. After the software performs image processing, and upon receiving an input selection from the operator, the software commands the syringe pump via a USB serial connection. The pump, which receives continuous feedback from the software, controls the actuation of the robot and the pressure is monitored to ensure safety. This entire system is represented in Fig. S1.

3.3.2 System Software

An anatomical model (Bronchoscopy Training Model 50-191, WorldPoint), typically used for surgical training purposes, was used for testing (*in-vitro*) the proposed soft surgical robotic platform (Fig. 2, A). To produce usable images to aid navigation tasks in the lung and perform robotic-assisted stabilization in front of a lesion, several image processing steps are executed (Fig. 2, B). First, a contour tracking algorithm was developed to enable the soft robot to recognize branches in the lung and automatically steer towards them to allow navigation. Images obtained from the micro camera are captured by the Magewell frame grabber as a Red-Green-Blue (RGB) image, passed to an OpenCV `Mat` object, and then converted to grayscale. To improve the contrast between a bronchial passage and the lumen wall, histogram equalization is performed, then a median filter is applied to remove image grain. This resulted in smooth contours that is converted to regions the software identifies as bronchial passages and subse-

quently tracks between frames as the robot moves. This procedure, called binary thresholding, produces the final contour shapes that the robot tracks. Eq. 1 is used to determine if a pixel would be converted to black or white, where the value T is the user-selected threshold value, and the coordinates (x, y) are the gray-scale pixel values from the median filter image.

$$(x, y)_{\text{out}} = \begin{cases} 255, & \text{if } (x, y)_{\text{in}} \leq T \\ 0, & \text{else} \end{cases} \quad (1)$$

To determine the center of mass of the target contour (\bar{x}, \bar{y}) in the local image-coordinate system where $(0, 0)$ corresponds to the top-left corner of the image, the OpenCV function `findContours` is used. The center of mass of the contour region is calculated (in pixels) by using the OpenCV `moments` function (referring to moments of area) and using Eq. 2, where M_{00} is the total area of the contour, M_{10} is the moment in the x direction (horizontal), and M_{01} is the moment in the y direction (vertical).

$$\bar{x} = \frac{M_{10}}{M_{00}}, \quad \bar{y} = \frac{M_{01}}{M_{00}} \quad (2)$$

The robot tip position is autonomously controlled via syringe pump actuation, that is based on live image processing of a continuous micro camera feed from the device tip that controls the alignment of the device to a branch of the lung. The robot can be automatically steered (with the embedded distally actuated one DOF) to align to a specific branch of the lung and then pushed and rotated manually from outside the patient to enter the branch.

To account for potential changes in lighting and contrast inside the lung model, an adaptive threshold algorithm that dynamically adjusts the threshold value was developed. The basic function of this algorithm is to automatically adjust the threshold to an optimal value that removes extraneous contours from the processed images. To execute this procedure, the software uses a buffer array of ten elements to log the number and location of contours found in each frame. The threshold value is increased if the number of contours found is zero; or if the buffer

array is filled and all the elements of the array are within one value of each other. Otherwise, the threshold is decreased if the array is filled and the values are not within one value of each other. The threshold is also decreased if the area of any contour found in an image has fewer than a 10 pixel-square area, since this indicates noise in the image and can be eliminated.

Another embedded feature of the software is its ability to track an object of interest inside the lung. During a bronchoscopy procedure in which a biopsy or drug delivery must occur, it is critical to maintain alignment of the soft robot and its tools relative to potentially cancerous lesions. Thus, an optimized template tracking algorithm from the OpenCV function `matchTemplate` was utilized, which allows a user to select an object of interest that is continuously tracked by tracing a box around the target. The algorithm, which is expressed in Eq. 3, performs the sum of the squared difference (SSD) technique for feature tracking:

$$SSD[x, y] = \sum_{p=0}^m \sum_{q=0}^n (I_1[p, q] - I_2[x + p, y + q])^2 \quad (3)$$

where I_1 is the template image, I_2 is the target image, (m, n) are the number of pixels in the template image corresponding to the horizontal and vertical size of the template image, respectively (which are known from the box traced by the user), and (x, y) are the pixels of the target image. The template is moved over the target image and the pixel values are subtracted pixel by pixel. The sum of the squares of these subtracted values returns the score for the current region, where the best match corresponded to the lowest score. The maximum cost of our feature tracking algorithm is ≈ 0.4 ms/frame when template tracking compared to no tracking tasks, see *Supplementary Information* and Table S1. In this application, the target is considered “centered” if the center of the box is within ± 2 pixels from the center of the image. In order to account for the radial distortion of the camera, a calibration method was implemented using Matlab, see *Supplementary Information* and Fig. S2. Additionally, a pixel to mm conversion procedure was implemented to improve results readability, see *Supplementary Information* and

Fig. S3.

3.4 Surgical Workflow

The surgical workflow for the proposed system will involve the following steps: 1) positioning the bronchoscope to a desired site in the bronchial tree; 2) deploying the soft robot from the endoscope working channel to the bronchial wall, and navigating through the smaller cavities of the peripheral lung to the target lesion, using direct visual feedback from the integrated micro camera and the on-board actuation mechanism to steer the robot tip as necessary; 3) once reached the surgical area of interest, the clinician can push the system to puncture lung tissue with the biopsy needle and enter the spongy lung parenchyma to perform a biopsy applying suction through the channel and aspirating biological material; 4) if necessary, fluids and/or drugs will be released into the lesion via the other delivery needle. Step 1) can be skipped, if so desired by the clinician, and the soft robot can be used as a stand-alone system, as the vision probe does not need to be removed when performing surgical tasks.

4 Results

This section covers testing methodologies implemented and characterizations results for the soft robot and the image capture and control system.

4.1 Lung tissue puncturing force characterization

Since forces required to puncture lung tissue are not known in the literature, we performed *ex-vivo* tests (Fig. 3) to evaluate them and designed our system so that it could meet this specific clinical requirement. The test was carried out on explanted porcine lung tissue (Fig. 3, A), sliced to expose different anatomical structures: 1) the spongy tissue of the lung, which contains a homogeneous network of micro-scale bronchioles and alveoli (Fig. 3, B), and 2) the

stiffer tissue that makes up larger bronchial passages (Fig. 3, C). Tests were repeated five times on each specimen. A 30 G needle was attached to an Instron testing machine (5943 Instron, USA) and pushed into the tissue at a rate of 0.5 mm/s while collecting force data, which were subsequently analyzed to determine the maximum force needed to puncture through the two different types of tissue. The average puncture force of the bronchial wall tissue was determined to be $430 \text{ mN} \pm 44 \text{ mN}$. The average force required to puncture the spongy tissue was $88 \text{ mN} \pm 18 \text{ mN}$. Because we are interested in performing diagnosis and therapy of lesions in peripheral lung locations (*i.e.*, where the tissue is predominantly spongy), we set this last value to be the target puncture force for our soft robot.

4.2 Finite Element Analysis

We modeled the soft robot behavior upon actuation using Abaqus (Simulia, Dassault Systems) in order to guide the design of the robot (specifically, its working channels and actuation chamber), predict the robot behavior upon pressurization, and evaluate areas of maximum deformation. The properties of the constituent material (Dragon Skin 00-10) of the robot were experimentally characterized using a tensile test dogbone that was subjected to a uniaxial tensile test on the Instron materials testing machine (using test parameters according to ASTM D412-16) to determine the engineering stress and strain behavior. For our FEA experiments, we fit the testing data in Abaqus to the third order hyperelastic Yeoh model (45, 46), see *Supplementary Information*. A comparison between this model and the experimental tensile test data is shown in Fig. S4, in order to provide the accuracy of the Yeoh model fit to the experimental data within the range of strain of the robot.

In the FEA, the device was subjected to a uniform static gravity load and a uniform static pressure load within its actuation chamber. A hexahedral mesh with quadratic geometric order and a hybrid element type was utilized with a global seed size of 0.24 mm. These parameters

generated 14,945 individual C3D20 hybrid elements.

The modeled robot was successfully simulated up to an actuation pressure of 66 kPa. An image comparing the model results to the actual performance of the device is shown in Fig. 4 and in Movie S1. The simulation captures the behavior of the robot upon pressurization (Fig. 4, B). This model provides insight into both the actuation chamber deformation and how its expansion affects the shape of the working channels (Fig. 4, A), which allows for the FEA to guide and validate the design of these microchannels. The size of the actuation chamber of the model and robot under no deformation is 0.36 mm and the working channels are 0.56 mm in diameter. As the chamber is pressurized the gap between the actuation chamber and working channels decreases. This progresses until approximately 56 kPa in the simulation, at this point the actuation chamber is closer to 0.72 mm in diameter and the working channels have less than a 2% change in overall shape, consequently the internal gap of the aforementioned channels is now comparable in size to the gap between the actuation chamber and the outer surface of the device. Due to this, the chamber begins expanding more evenly between the outer surface and the internal chambers, thus more significantly distorting the working channels as pressure continues to increase. Upon reaching the maximum pressure simulated, the actuation chamber deforms to a diameter of 1.50 mm and the working channels become more severely deformed ellipses with approximate major and minor axis of 0.71 mm and 0.43 mm, respectively. However, the working channels remain undeformed at the infilled silicone plugged ends of the actuation chamber, thus retaining original shape at the distal end of the device. This is considered satisfactory since the distal end is where the micro camera and interventional tools (biopsy and delivery needles) are integrated. The working channels only integrate the micro camera cable and tubing (for biopsy and delivery needles) along their length, which are significantly smaller in diameter compared to the microchannels. We also used FEA simulations to compare the retroflexion of the robot with integrated needles and micro camera to the physical device (see Fig. S5).

4.3 Blocked Force

We evaluated blocked force for the soft robot. The Instron testing machine, equipped with a 50 N load cell (PN 2530-50 N), was used to collect force data. Input pressure was measured with the pressure sensor connected to the Instron's DAQ, which recorded data in parallel with the Instron. During each test, one side of the robot was fixed with a frame and the other was constrained under the Instron load cell in a straight configuration (0° bending), as shown in Fig. S6. Similarly to (47), the entire length of the robot was constrained (the robot is positioned in the setup such that the actuation chamber is on the bottom) to minimize nonlinear effects (i.e., the tendency of the robot to bend when pressurized) and to concentrate the force at the distal tip. Testing was conducted on three different soft robots. For this experiment, force data was sampled every 1 kPa until the robots failed due to rupture of their actuation chambers. The experimental results from this test are reported in Fig. 5, A. The mean maximum blocked force resulted in 0.47 N with a standard deviation of ± 0.097 N.

4.4 Bending Angle

We evaluated the maximum bending angle of the soft robot by tracking different samples' trajectories using images taken from a camera during unloaded pressurization. First, the syringe pump, connected via USB to a computer running a Python script, was connected to the actuation chamber. Air was injected into the actuation chamber at a flow rate of 5 mL/min to simulate quasi-static conditions and each test was repeated three times. During each test, one side of the device was constrained and the other was left free to move. The robot was positioned horizontally. The actuation pressure was monitored with the pressure sensor, and data was collected via a Teensy 3.2 microcontroller with 10-bit resolution (PJRC, USA). Photographs were taken with a DSLR camera (Nikon D7500, Japan), the shutter of which was triggered remotely by the microcontroller, at predetermined discrete pressure values. Finally, after the image data was

collected, Matlab (Mathworks, USA) was used to determine the bending angle at each pressure step, according to the schematic of Fig. S7.

The data resulting from this test are shown in Fig. 5, B. The system requires an initial minimum pressure before the bending can start, which is ≈ 50 kPa. After reaching this pressure, a small pressure increase is necessary to achieve full bending. Results show that the soft robot is capable of bending up to 253° (upon pressurization up to 85 kPa), thus beyond full retroflexion (*i.e.*, 180°). Similar pressure ranges are typically used in soft surgical robots currently being investigated in the literature, please refer to the following review papers (35–37). Finally, the bending angle testing results were compared to the FEA results to further validate the system design (see Fig. S8).

4.5 Angular velocity

We assessed the angular velocity of the soft robot by tracking three different samples' trajectories using images taken from a camera during unloaded pressurization up to 85 kPa. The results from these tests are shown in Fig. 5, C. This experiment was performed using four different flow rates from the syringe pump in the range of 20-80 mL/min. Angular velocity was computed using angular position data (obtained with the same method described in Section 4.4) and the recorded time interval between each photograph as: $\dot{\theta} = \frac{\theta_i - \theta_{i-1}}{t_i - t_{i-1}}$, where i represents the index position within an array of recorded pressure steps. Results (Fig. 5, C) show a tunable and controllable speed from 12.3 ± 3.30 °/s (corresponding to a 20 mL/min flow rate) up to 43.7 ± 3.54 °/s (corresponding to a 80 mL/min flow rate). Angular velocities corresponding to 40 mL/min and 60 mL/min flow rate are respectively 17.6 ± 3.90 °/s and 27.8 ± 5.00 °/s.

4.6 Robot Workspace

An optical motion capture system (OptiTrack, USA) was used to characterize the motion of the soft robot in free space. Reflective tape was wrapped around the tip of a robot (*i.e.*, distal end) and the proximal end. Then, the robot was actuated through its full range of motion. The system recorded Cartesian coordinate data that was later processed in Matlab to visualize the motion. Testing was performed with the robot hung downwards vertically, such that its center axis was perpendicular to the ground and the tip was closest to the ground. A series of five tests was performed up to a maximum pressure of 110 kPa, achieving over 270° bending. Test results are shown in Fig. 5, D. To best illustrate the performance, photos of the robot during testing are superimposed over the plot.

4.7 Soft robot *ex-vivo* testing

In this test, we assessed the interventional capabilities of the proposed soft robot *ex-vivo* on explanted porcine lung tissue specimens. To evaluate the capability of the system to perform lung tissue puncturing, which is necessary for diagnosis (*i.e.*, biopsies) and therapy (*i.e.*, targeted drug delivery), the soft robot with an integrated 30 G stainless steel needle (with a sharp 75° profile cut) was used to puncture lung tissue and inject it with dyed water. The spongy tissue was obtained by resecting transverse cross sections of the lung, each approximately 2 cm thick. The tissue was assumed to be approximately homogeneous, so puncture sites were chosen randomly. The robot was setup on the Instron testing machine such that, if a puncture was successful, it could inject a solution of dyed water into the spongy tissue, thus producing a visible indication of successful puncture. The average force required to puncture the tissue was $48 \text{ mN} \pm 7.9 \text{ mN}$. We demonstrated the capability of the system to puncture lung tissue and perform diagnostic and therapeutic tasks by *in-situ* delivery of a drug model. The dye indications from these successful punctures and injections can be seen in Fig. 6 and Movie S1.

4.8 Navigation and Tracking Tasks

This section details the performance characterization of the image-guided control system. For all tests, the soft robot with the integrated micro camera was inserted in the 3D bronchoscopy training model (Fig. 2, A), which served as an *in-vitro* lung model. A schematic of the test setup using the lung model is shown in Fig. S9.

4.8.1 Navigation: Contour Tracking

The two inputs that have the greatest effect on the shape and ability of the system to find contours representing lung branches, are the size of the median filter and the magnitude of the threshold cutoff value. The robot was inserted into the lung model and images are taken and then processed with different combinations of median filter sizes and threshold values to determine the effect on finding contours and evaluate the performance of the contour tracking ability. The operator selected the contour, commanding the robot to align to the contour's center of mass. The software logged the elapsed time and the tracking error, *i.e.* the difference between the actual coordinate position of the camera and the coordinate position of the contour's center of mass. This data was then exported to be evaluated in Matlab. The same contour was tracked for each test, and the device was reset to its original position after every run. With one DOF, the camera is able to track and align a selected branch to the middle of the frame in either the horizontal or vertical plane. In the tests performed, the center of mass of the contour was aligned with the middle of the image in the vertical plane. Once a contour is chosen, the location of the contours center of mass is subtracted from the center of the image and the robot is instructed on which way to move. An overview of how the tracking works is shown in Fig. 7, A. After a branch contour has been selected, the system state is changed from *STOP* to *CENTER_CONTOUR*. The closest contour to the mouse click, found via the Euclidean distance, becomes the contour of interest to be tracked. A global X,Y variable corresponding to

the center of mass of this contour is updated with these coordinates. During every frame, a contour is searched for in the immediate (5-pixel area) region around these global coordinates. If a contour's center of mass is found, the global coordinates are updated to reflect the movement of this contour. Once a contour is found, it is inserted into a list that keeps track of the contour ID and the frame it was found in and a future frame is designated to be the frame where the contour will be removed from the list if the contour is not found again. If the contour to be centered is removed from the list, the system will stop and change state to *STOP*.

The results (Fig. 7, B) show that if the threshold value is too small, the computer vision algorithm may find peripheral contours of branches that are too far down a bronchial passage, and a too high threshold value caused the contours to blend in with other features (*e.g.*, bronchial wall). Furthermore, if the median filter value was too small, the contour appeared to be noisier, consisting of many overlapping and smaller contours; and if it was too large, it began to eliminate contours that had a small area. Threshold values between 20 and 40 pixels, and median filter sizes between 15 and 37 pixels produced viable results for most scenarios.

4.8.2 Navigation: Adaptive Threshold

The adaptive threshold procedure was characterized inside the lung model by initiating the contour tracking logic with an extremely high or low threshold value that, effectively, rendered the contour tracking unusable. The software was then commanded to optimize the threshold value. Dynamic thresholding allows for the software to determine a threshold value that is able to find the contours of the branch automatically. The soft robot was tested five times for both low and high threshold values, resulting in ten total tests.

The results for an image using the dynamic thresholding are shown in Fig. 8. The system tended to converge to the same threshold value in all tests, regardless of whether the threshold value is increasing or decreasing. The threshold value converged faster when threshold value

was initially high, because the conditions to decrease the threshold were easier to meet than the conditions to increase it. This is because, when evaluating if there is noise in the image, if any of the contours have a pixel area less than 10, the threshold is immediately decreased and the buffer array is restarted. However, to increase the threshold, there either needs to be zero contours found in the image, or 10 successive frames where all the value of the elements in the buffer array are within one from each other. This can be seen in the step like trend of the increasing threshold data series before it reaches the final value as certain frames are not increasing the threshold as the buffer is not full. The dynamic threshold will stabilize right on the edge of noise and will constantly be trying to update through a procedure.

4.8.3 Navigation: Robotic-assisted navigation

To evaluate the tracking speed of the robot, four pump injection rates between $1.5^{\circ}/s$ and $8.2^{\circ}/s$ were tested, and a single system was tested three times for each of these rates. Results are shown in Fig. 9, A. The error is defined as the difference from the middle of the image to the center of the contour that is being tracked, with the aim of the operation being to drive the error to zero. Faster injection rates resulted in a faster tracking time, but caused the robot to overshoot the contour before settling (see Movie S1). For our purposes, we defined settling time to be the time the system took to stabilize at the target location within an error of ± 2 px starting from the time that the initial position error begins decreasing. This settling time varied with angular velocity and we found the mean maximum and mean minimum settling times to be 30.2 s and 8.46 s for $1.5^{\circ}/s$ and $8.2^{\circ}/s$, respectively (Fig. 9, A). Additionally, for these maximum and minimum angular velocities, the mean overshoot amount past alignment of 2 px positional error (target is considered the bounds of 2 px error for overshoot) was 0.996 mm and 0.175 mm, respectively. Due to the 4 px (± 2 px) span of positions considered aligned, the system will continue to track and align to avoid substantial steady-state error. These values can be controlled by using

different angular velocities or changing the bounds of the pixels that are considered aligned to meet clinical requirements and could vary depending on the tracking capabilities required for each patient. In all cases, the soft robot is able to reach the target position, even if the system overshoot. At this point, the robot can be inserted in the desired lung branch.

4.8.4 Stabilization in front of a lesion: Template Tracking

During a bronchoscopy procedure, it is common for a lesion to move slightly due to the clinician moving the bronchoscope or the patient breathing. Thus, it is important for the robot to be able to re-align to the lesion in order to adjust for these small movements. Similar to the contour tracking test, an object of interest was selected to evaluate the template tracking capabilities of the system. In this case, a 7 mm diameter dyed paper ball was used as an analog for a lesion. When the system is told to perform a lesion tracking procedure, it will center the lesion to the vertical center of the camera and maintain this positioning even if the lesion moves off the center line. To start the lesion tracking, the operator must first draw a box around the lesion or area of interest using the mouse. The area selected becomes the template image for a template tracking procedure. Once the mouse button is released, the system will align the middle of the box to the center of the image. The lesion will be considered centered if the center of the box is within ± 2 pixels from the center of the image. Once a lesion is selected by the user, the system will center the lesion to the vertical center of the image and maintain this positioning even if the lesion moves off the center line (*i.e.*, by actuating the robot) – see Movie S1.

A graph of the error and pressure variation versus time for lesion tracking is shown in Fig. 10, A. The variation of the pressure response during all navigation and tracking tasks is consistent with the results shown in Fig. 10 with minor differences in overshoot and settling time depending on the angular velocity (see Fig. S10). For this test, the robot was actuated at an angular velocity of $3.2^\circ/\text{s}$. Once the lesion was centered in the frame, the system was

perturbed several times to verify that the system was capable of recognizing the location of the lesion and re-align to it (Fig. 10, B). Perturbations were done by manually moving the system from the outside of the anatomical model. The figure shows that, despite the disruptions to the alignment, the system was capable of re-aligning the robot to the lesion and hold this position. The error is defined as the difference from the middle of the image to the middle of the lesion's box, as such the error will be positive if the middle of the box is to the left of the center of the image and negative if the middle of the box is to the right of the center of the image. The green shaded region on the graph represents the region for 0 ± 2 pixels (0.180 mm) which is when the lesion is considered centered. As in the contour tracking this pixel value was converted to a millimeter value utilizing the method described above.

5 Conclusion

We have designed, modeled, and fabricated a 2.4 mm soft robot, with vision-based navigation capability as well as diagnostic and therapeutic capabilities, to treat early stage lung cancer. The system is designed with the intent of improving access and treatment options in peripheral regions of the lung. We have performed mechanical characterizations of the robotic platform and assessed its performance in *in-vitro* and *ex-vivo* experiments to ensure it would meet clinical requirements. Our technology enables low-cost batch manufacturing, thus paving the way for disposable miniaturized soft surgical robots, with the benefit of reducing number of uses and reduce risks associated with material aging, wear, and breakage after repeated use. Since health care associated infections are an important source of morbidity and mortality, a disposable surgical robot has the potential to help reduce these risks and the related high cost for sterilization and disinfection of instruments (which can also cause material damage). The only component of the robot that is not disposable is the micro camera, which can be removed from the robot working channel, cleaned, and disinfected. Another advantage of our system is distal

soft fluidic actuation, which can ensure safe interaction with biological tissue, as opposed to other small-scale actuators like piezoelectric bimorph and shape memory alloys – that require high voltage or current to operate (48–50), and no loss due to friction or backlash.

Our results show the suitability of the proposed system for interventional bronchoscopy applications. We have modeled the soft robot behavior upon actuation and assessed the performance of the robot through experimental characterizations of blocked force, deflection, velocity, and 3D workspace. The soft robot is capable of bending up to 253° , thus beyond full retroflexion and outperforming capabilities of current commercial bronchoscopes. For example, video bronchoscopes manufactured by Olympus and Pentax, two major manufacturers of endoscopic devices, are reported to be capable of bending up to $\approx 180^\circ$ (6, 7). The proposed device has the potential to augment dexterity in interventional bronchoscopy and aid in complex navigation tasks in peripheral areas of the lungs, where the angles of the various takeoffs of the bronchi can be difficult to navigate and bronchi branches are difficult to reach, such as apical segments. Angular velocity characterizations showed a tunable controllable speed up to $45^\circ/\text{s}$. Evaluation of 3D reachable workspace of the robot in free motion showed repeatability and accuracy of the robot. We demonstrated the interventional capabilities of the proposed soft robot *ex-vivo* on explanted porcine lung tissue specimens, including the capability to perform lung tissue puncturing to perform diagnosis (i.e., biopsies) and therapy (i.e., targeted drug delivery).

The system is capable of performing robotic-assisted navigation in deep peripheral lung locations in *in-vitro* conditions (i.e., using a 3D bronchoscopy training model) through an on-board micro camera and a dedicated computer vision algorithm, that allows the clinician to select the bronchial branch they want to navigate into through a GUI and steers the robot automatically (see Movie S1). The computer vision algorithm is based on a dynamic threshold function to automatically find a suitable threshold cut-off value needed for identifying branch contours in the bronchial tree. This function can be tuned by the clinician on-the-fly via the

GUI to select smaller branches as they move deeper in the lung, thus providing an easy-to-use navigation and guidance system. Navigation is performed under visual guidance at all times throughout the procedure, since there is no need to remove the embedded micro camera to insert additional interventional tools. The soft robot is capable of performing robotic-assisted stabilization in front of a lesion during a simulated procedure in an *in-vitro* experiment. This is achieved through a function embedded in our computer vision algorithm that enables automated tracking and aligning to a lesion. Through the GUI, the clinician is able to locate and identify a lesion and instruct the robot to track it as well as center and stabilize itself with respect to the lesion (*i.e.*, target surgical area) in real-time, so that it can hold its position to perform a biopsy or deliver a drug, and recover its position centered in front of the lesion when perturbed.

The proposed system is a miniaturized soft surgical robot able to access peripheral lung locations. It will pave the way towards simultaneous diagnostic and therapeutic capabilities (*i.e.*, within the same bronchoscopy procedure) in early stage lung cancer treatment, with the aid of digital microscopy techniques and on-site pathology. This can potentially shorten current delays in diagnosis and treatment and become a promising approach towards battling lung cancer. Future works include: 1) improving the robot angular velocity by increasing the fluid injection rate, developing a dedicated electropneumatic control system, and using an incompressible fluid (*e.g.*, saline solution); 2) developing and integrating a distally-actuated needle deployment mechanism to avoid the need for the clinician to manually push the robot to puncture lung tissue; 3) integrating our image-guided approach with pre-operative CT imaging to plan navigation and identify the most effective and efficient path to the target lesion; and 4) validating the robot's safety and functionality in an *in-vivo* animal model.

6 Acknowledgments

The authors gratefully acknowledge support by the Lung Cancer Initiative at Johnson and Johnson. In particular, we thank Dr. Hannah McEwen for providing technical and clinical feedback and guidance.

References and Notes

1. R. L. Siegel, K. D. Miller, and A. Jemal, “Cancer statistics, 2020,” *CA: A Cancer Journal for Clinicians*, vol. 70, no. 1, pp. 7–30, 1 2020. [Online]. Available: <https://onlinelibrary.wiley.com/doi/abs/10.3322/caac.21590>
2. E. Billatos, J. L. Vick, M. E. Lenburg, and A. E. Spira, “The airway transcriptome as a biomarker for early lung cancer detection,” pp. 2984–2992, 7 2018. [Online]. Available: <http://www.ncbi.nlm.nih.gov/pubmed/29463557>
3. R. Maconachie, T. Mercer, N. Navani, and G. Mcveigh, “Lung cancer: Diagnosis and management: Summary of updated NICE guidance,” *The BMJ*, vol. 364, 2019. [Online]. Available: <https://pubmed.ncbi.nlm.nih.gov/30923038/>
4. M. P. Rivera, A. C. Mehta, and M. M. Wahidi, “Establishing the diagnosis of lung cancer: Diagnosis and management of lung cancer, 3rd ed: American college of chest physicians evidence-based clinical practice guidelines,” *Chest*, vol. 143, no. 5 SUPPL, 5 2013.
5. W. J. Heerink, G. H. de Bock, G. J. de Jonge, H. J. Groen, R. Vliegenthart, and M. Oudkerk, “Complication rates of CT-guided transthoracic lung biopsy: meta-analysis,” *European Radiology*, vol. 27, no. 1, pp. 138–148, 1 2017.
6. “Olympus Global Homepage.” [Online]. Available: <https://www.olympus-global.com/>

7. “PENTAX Medical (Global).” [Online]. Available: <https://www.pentaxmedical.com/pentax/>
8. V. Vitiello, Su-Lin Lee, T. P. Cundy, and Guang-Zhong Yang, “Emerging Robotic Platforms for Minimally Invasive Surgery,” *IEEE Reviews in Biomedical Engineering*, vol. 6, pp. 111–126, 2013. [Online]. Available: <http://ieeexplore.ieee.org/document/6392862/>
9. A. Loeve, P. Breedveld, and J. Dankelman, “Scopes Too Flexible...and Too Stiff,” *IEEE Pulse*, vol. 1, no. 3, pp. 26–41, 11 2010. [Online]. Available: <http://ieeexplore.ieee.org/document/5642168/>
10. “Robotic Endoscopy - Auris Health.” [Online]. Available: <https://www.aurishealth.com/>
11. “Intuitive | Robotic-Assisted Bronchoscopy | Ion Platform.” [Online]. Available: <https://www.intuitive.com/en-us/products-and-services/ion>
12. “superDimension™ Navigation System | Medtronic.” [Online]. Available: <https://www.medtronic.com/covidien/en-us/products/interventional-lung-solutions/superdimension-navigation-system.html>
13. J. Burgner, D. C. Rucker, H. B. Gilbert, P. J. Swaney, P. T. Russell, K. D. Weaver, and R. J. Webster, “A telerobotic system for transnasal surgery,” *IEEE/ASME Transactions on Mechatronics*, vol. 19, no. 3, pp. 996–1006, 2014. [Online]. Available: [/pmc/articles/PMC4118753/?report=abstracthttps://www.ncbi.nlm.nih.gov/pmc/articles/PMC4118753/](https://www.ncbi.nlm.nih.gov/pmc/articles/PMC4118753/?report=abstracthttps://www.ncbi.nlm.nih.gov/pmc/articles/PMC4118753/)
14. J. Burgner-Kahrs, D. C. Rucker, and H. Choset, “Continuum Robots for Medical Applications: A Survey,” *IEEE TRANSACTIONS ON ROBOTICS*, vol. 31, no. 6, p. 1261, 2015. [Online]. Available: <http://ieeexplore.ieee.org>.

15. J. Sganga, D. Eng, C. Graetzel, and D. Camarillo, “Offsetnet: Deep learning for localization in the lung using rendered images,” in *Proceedings - IEEE International Conference on Robotics and Automation*, vol. 2019-May, 5 2019, pp. 5046–5052.
16. Z. Zhao, S. Jordan, and Z. T. H. Tse, “Devices for image-guided lung interventions: State-of-the-art review,” *Proceedings of the Institution of Mechanical Engineers, Part H: Journal of Engineering in Medicine*, vol. 233, no. 4, pp. 444–463, 4 2019.
17. B. Yu, J. D. G. Fernández, and T. Tan, “Probabilistic Kinematic Model of a Robotic Catheter for 3D Position Control,” *Soft Robotics*, vol. 6, no. 2, pp. 184–194, 4 2019.
18. M. Jolaei, A. Hooshir, J. Dargahi, and M. Packirisamy, “Toward Task Autonomy in Robotic Cardiac Ablation: Learning-Based Kinematic Control of Soft Tendon-Driven Catheters,” *Soft Robotics*, 7 2020.
19. J. B. Gafford, S. Webster, N. Dillon, E. Blum, R. Hendrick, F. Maldonado, E. A. Gillaspie, O. B. Rickman, S. D. Herrell, and R. J. Webster, “A Concentric Tube Robot System for Rigid Bronchoscopy: A Feasibility Study on Central Airway Obstruction Removal,” *Annals of Biomedical Engineering*, vol. 48, no. 1, pp. 181–191, 1 2020. [Online]. Available: <https://pubmed.ncbi.nlm.nih.gov/31342337/>
20. P. J. Swaney, A. W. Mahoney, B. I. Hartley, A. A. Ramirez, E. Lamers, R. H. Feins, R. Alterovitz, and R. J. Webster, “Toward Transoral Peripheral Lung Access: Combining Continuum Robots and Steerable Needles,” *Journal of Medical Robotics Research*, vol. 02, no. 01, p. 1750001, 3 2017. [Online]. Available: <http://www.worldscientific.com/doi/abs/10.1142/S2424905X17500015>
21. A. Gao, N. Liu, M. Shen, M. E.M.K. Abdelaziz, B. Temelkuran, and G.-Z. Yang, “Laser-Profiled Continuum Robot with Integrated Tension Sensing for Simultaneous

Shape and Tip Force Estimation,” *Soft Robotics*, 2 2020. [Online]. Available: <https://pubmed.ncbi.nlm.nih.gov/32077810/>

22. Y. Watanabe, M. Maeda, N. Yaji, R. Nakamura, and H. Iseki, “Small, soft, and safe microactuator for retinal pigment epithelium transplantation,” in *2007 IEEE 20th International Conference on Micro Electro Mechanical Systems (MEMS)*, no. January. IEEE, 1 2007, pp. 659–662.
23. H. Okayasu, Jun Okamoto, M. Fujie, and H. Iseki, “Development of a Hydraulically-driven Flexible Manipulator Including Passive Safety Method,” in *Proceedings of the 2005 IEEE International Conference on Robotics and Automation*, vol. 2005, no. April. IEEE, 2005, pp. 2890–2896.
24. M. Cianchetti, T. Ranzani, G. Gerboni, T. Nanayakkara, K. Althoefer, P. Dasgupta, and A. Menciassi, “Soft Robotics Technologies to Address Shortcomings in Today’s Minimally Invasive Surgery: The STIFF-FLOP Approach,” *Soft Robotics*, vol. 1, no. 2, pp. 122–131, 6 2014. [Online]. Available: <http://online.liebertpub.com/doi/abs/10.1089/soro.2014.0001>
25. T. Da Veiga, J. H. Chandler, P. Lloyd, G. Pittiglio, N. J. Wilkinson, A. K. Hoshier, R. A. Harris, and P. Valdastrì, “Progress in Biomedical Engineering Challenges of continuum robots in clinical context: a review. Challenges of continuum robots in clinical context: a review,” *Progress in Biomedical Engineering*, 6 2020.
26. Y. Huan, I. Tamadon, C. Scatena, V. Cela, G. A. Naccarato, A. Menciassi, and E. Sinibaldi, “Soft Graspers for Safe and Effective Tissue Clutching in Minimally Invasive Surgery,” *IEEE Transactions on Biomedical Engineering*, pp. 1–1, 5 2020.
27. D. Rus and M. T. Tolley, “Design, fabrication and control of soft robots,” *Nature*, vol. 521, no. 7553, pp. 467–475, 2015.

28. S. Russo, T. Ranzani, C. J. Walsh, and R. J. Wood, “An Additive Millimeter-Scale Fabrication Method for Soft Biocompatible Actuators and Sensors,” *Advanced Materials Technologies*, vol. 2, no. 10, p. 1700135, 10 2017.
29. N. Kumar, J. Wirekoh, S. Saba, C. N. Riviere, and Y.-L. Park, “Soft Miniaturized Actuation and Sensing Units for Dynamic Force Control of Cardiac Ablation Catheters,” *Soft Robotics*, 2020.
30. Y. Kim, G. A. Parada, S. Liu, and X. Zhao, “Ferromagnetic soft continuum robots,” *Science Robotics*, vol. 4, no. 33, p. eaax7329, 8 2019.
31. L. Hines, K. Petersen, G. Z. Lum, and M. Sitti, “Soft Actuators for Small-Scale Robotics,” *Advanced Materials*, vol. 29, no. 13, p. 1603483, 4 2017. [Online]. Available: <http://doi.wiley.com/10.1002/adma.201603483>
32. J. D. Greer, T. K. Morimoto, A. M. Okamura, and E. W. Hawkes, “A Soft, Steerable Continuum Robot That Grows via Tip Extension,” *Soft Robotics*, vol. 6, no. 1, pp. 95–108, 2 2019.
33. P. Polygerinos, N. Correll, S. A. Morin, B. Mosadegh, C. D. Onal, K. Petersen, M. Cianchetti, M. T. Tolley, and R. F. Shepherd, “Soft Robotics: Review of Fluid-Driven Intrinsically Soft Devices; Manufacturing, Sensing, Control, and Applications in Human-Robot Interaction,” *Advanced Engineering Materials*, vol. 19, no. 12, p. 1700016, 12 2017. [Online]. Available: <https://pdfs.semanticscholar.org/d8cd/ebdb57d9bc3f0d3039cc20ca425a7cb216f.pdf>
<http://doi.wiley.com/10.1002/adem.201700016>

34. A. . Faudzi, R. F. Surakusumah, D. E. Octorina Dewi, I. N. A. Mohd. Nordin, and M. R. Muhammad Razif, “Development of Flexible Bronchoscope Device Using Soft Actuator.” Springer, Singapore, 2015, pp. 223–241.
35. M. Cianchetti, C. Laschi, A. Menciassi, and P. Dario, “Biomedical applications of soft robotics,” *Nature Reviews Materials*, vol. 3, no. 6, pp. 143–153, 6 2018.
36. M. Runciman, A. Darzi, and G. P. Mylonas, “Soft Robotics in Minimally Invasive Surgery,” *Soft Robotics*, vol. 6, no. 4, 2019.
37. M. W. Gifari, H. Naghibi, S. Stramigioli, and M. Abayazid, “A review on recent advances in soft surgical robots for endoscopic applications,” *The International Journal of Medical Robotics and Computer Assisted Surgery*, vol. 15, no. 5, p. e2010, 10 2019. [Online]. Available: <https://onlinelibrary.wiley.com/doi/abs/10.1002/rcs.2010>
38. T. R. Gildea, S. D. Byfield, D. Kyle Hogarth, D. S. Wilson, and C. C. Quinn, “A retrospective analysis of delays in the diagnosis of lung cancer and associated costs,” *ClinicoEconomics and Outcomes Research*, vol. 9, pp. 261–269, 5 2017.
39. M. M. Jacobsen, S. C. Silverstein, M. Quinn, L. B. Waterston, C. A. Thomas, J. C. Benneyan, and P. K. Han, “Timeliness of access to lung cancer diagnosis and treatment: A scoping literature review,” pp. 156–164, 10 2017.
40. A. Bukhari, G. Kumar, R. Rajsheker, and R. Markert, “Timeliness of Lung Cancer Diagnosis and Treatment.” *Federal practitioner : for the health care professionals of the VA, DoD, and PHS*, vol. 34, no. Suppl 1, pp. 24S–29S, 2 2017. [Online]. Available: <http://www.ncbi.nlm.nih.gov/pubmed/30766298><http://www.pubmedcentral.nih.gov/articlerender.fcgi?artid=PMC6375422>

41. R. Myers and S. C. Lam, “Early Diagnosis of Lung Cancer,” in *Flexible Bronchoscopy*. Wiley, 5 2020, vol. 22, no. 2, pp. 127–136.
42. M. Andolfi, R. Potenza, R. Capozzi, V. Liparulo, F. Puma, and K. Yasufuku, “The role of bronchoscopy in the diagnosis of early lung cancer: A review,” *Journal of Thoracic Disease*, vol. 8, no. 11, pp. 3329–3337, 2016.
43. Y. Umeda, M. Otsuka, H. Nishikiori, K. Ikeda, Y. Mori, T. Kobayashi, Y. Asai, Y. Takahashi, Y. Sudo, K. Kodama, G. Yamada, H. Chiba, and H. Takahashi, “Feasibility of rapid on-site cytological evaluation of lung cancer by a trained pulmonologist during bronchoscopy examination,” *Cytopathology*, vol. 30, no. 6, pp. 628–633, 11 2019. [Online]. Available: <https://onlinelibrary.wiley.com/doi/abs/10.1111/cyt.12771>
44. H. J. Soukiasian, “Surgery soon after clinical staging of non-small cell lung cancer reduces cancer progression and improves likelihood of cure,” in *American Association for Thoracic Surgery - AATS 98th Annual Meeting*, 2018.
45. O. H. Yeoh, “Some forms of the strain energy function for rubber,” *Rubber Chemistry and Technology*, vol. 66, no. 5, pp. 754–771, 11 1993.
46. L. Marechal, P. Balland, L. Lindenroth, F. Petrou, C. Kontovounisios, and F. Bello, “Toward a Common Framework and Database of Materials for Soft Robotics,” *Soft Robotics*, 6 2020. [Online]. Available: <https://www.liebertpub.com/doi/abs/10.1089/soro.2019.0115>
47. P. Polygerinos, Z. Wang, J. T. B. Overvelde, K. C. Galloway, R. J. Wood, K. Bertoldi, and C. J. Walsh, “Modeling of Soft Fiber-Reinforced Bending Actuators,” *IEEE Transactions on Robotics*, vol. 31, no. 3, 2015.
48. J. Gafford, T. Ranzani, S. Russo, A. Degirmenci, S. Kesner, R. Howe, R. Wood, and C. Walsh, “Toward Medical Devices With Integrated Mechanisms, Sensors, and Actua-

tors Via Printed-Circuit MEMS,” *Journal of Medical Devices*, vol. 11, no. 1, p. 011007, 1 2017.

49. J. B. Gafford, T. Ranzani, S. Russo, H. Aihara, C. Thompson, R. J. Wood, and C. J. Walsh, “Snap-on robotic wrist module for enhanced dexterity in endoscopic surgery,” in *2016 IEEE International Conference on Robotics and Automation (ICRA)*. IEEE, 5 2016, pp. 4398–4405.
50. M. Ho, A. B. McMillan, J. M. Simard, R. Gullapalli, and J. P. Desai, “Toward a meso-scale SMA-actuated MRI-compatible neurosurgical robot,” *IEEE Transactions on Robotics*, vol. 28, no. 1, pp. 213–222, 2 2012.

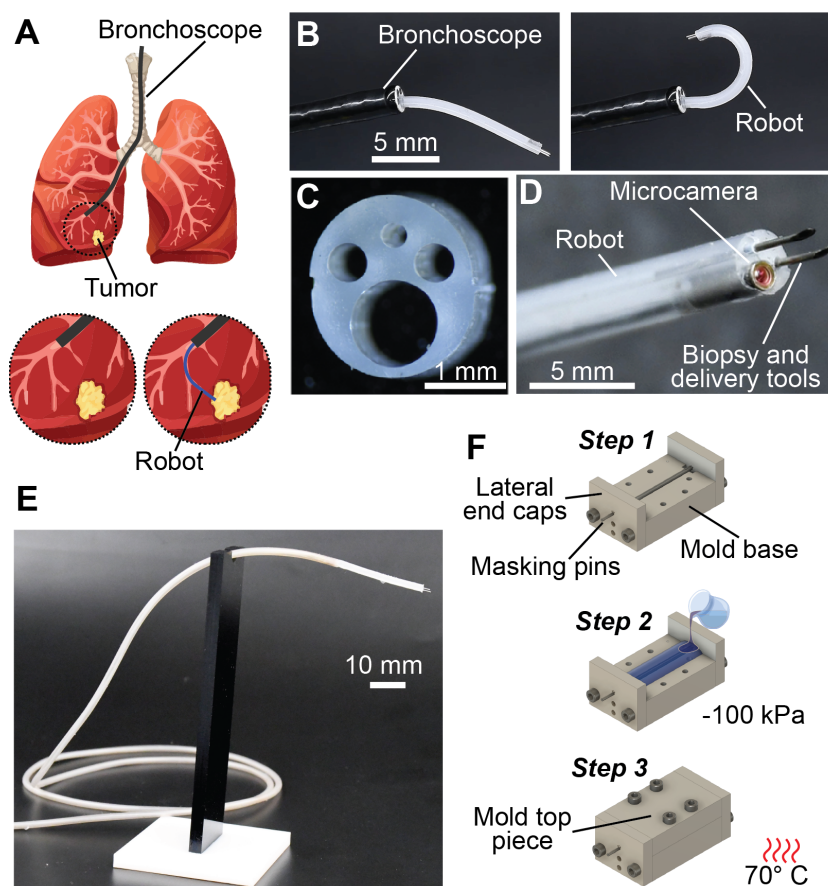


Figure 1: Proposed soft robot. A) Challenges in interventional bronchoscopy. Bottom: close-up view of the bronchoscope navigation limitations due to its size (left), and navigation capabilities of proposed miniaturized system (right). B) Robot integrated in the Olympus bronchoscope, with integrated biopsy and delivery needles and micro camera, demonstrating one DOF (actuating upwards) and performing complete retroflexion (180° bending). C) Robot frontal section after fabrication (without integrated micro camera and needles), showing its working channels. D) Close-up view of fully assembled system. E) Whole prototype. F) Fabrication steps.

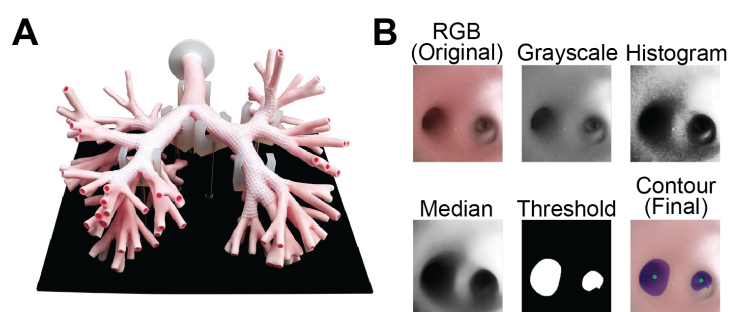


Figure 2: A) Anatomical lung model used for *in-vitro* testing. B) Image processing procedure. Bottom right: the contours are shown overlaid on top of the original image with the center of mass of each of the contours marked with a green dot.

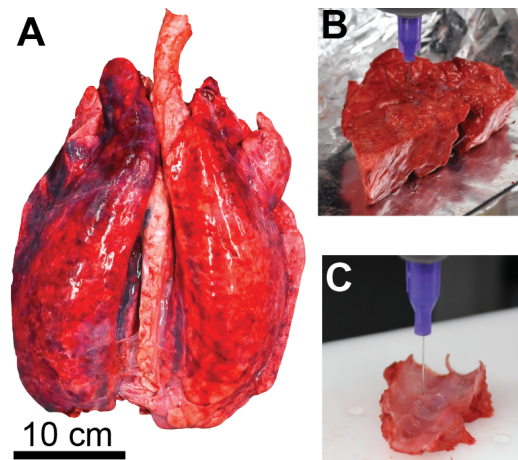


Figure 3: Lung tissue puncturing force characterization *ex-vivo* to find clinical requirements. A) Explanted porcine lung. B) Testing on resected spongy lung tissue. C) Testing on resected stiffer lung tissue. In both tests (B-C), a 30 G needle is attached to the Instron testing machine and positioned vertically, facing down towards the lung tissue.

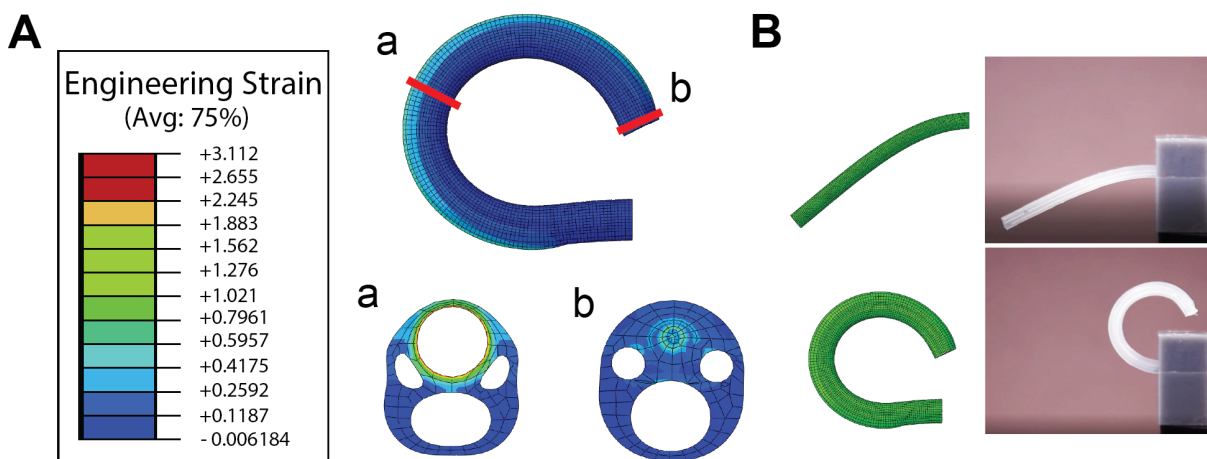


Figure 4: FEA of the soft robot during chamber pressurization and consequent actuation. A) Engineering strain of the device at full extension depicting the deformation of the cross section at: a) the midsection of the device and b) the tip of the device. The bending motion of the device does not alter the working channels at its distal tip. B) Bending of the device upon chamber pressurization (model versus physical testing).

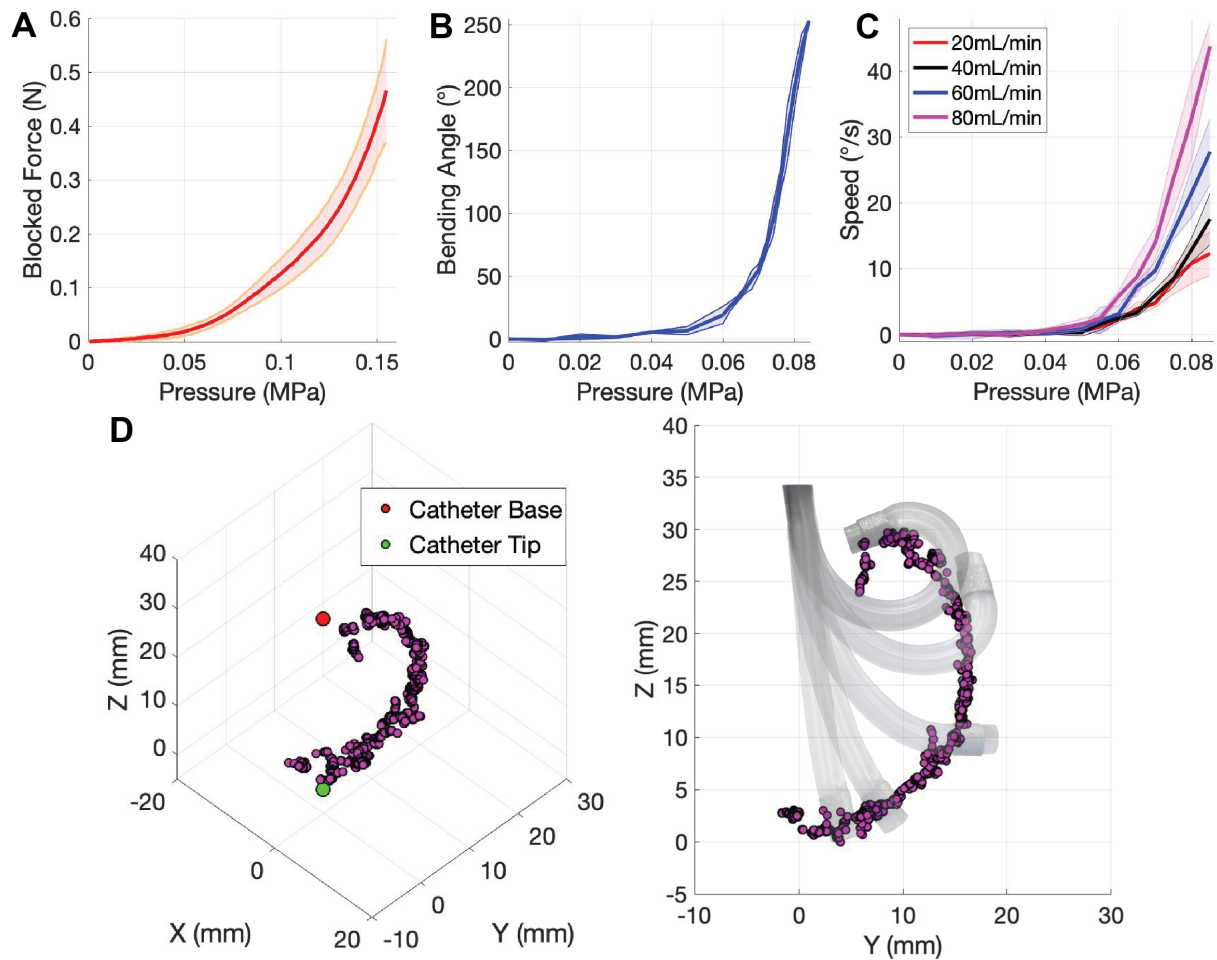


Figure 5: Soft robot performance characterizations. A) Blocked max force versus input pressure. B) Bending angle versus input pressure. C) Angular velocity versus input pressure, tested at four different flow rates. D) Robot workspace. In plots A-C, the solid line is the mean resulting from three experiments, and the shaded area is the standard deviation.

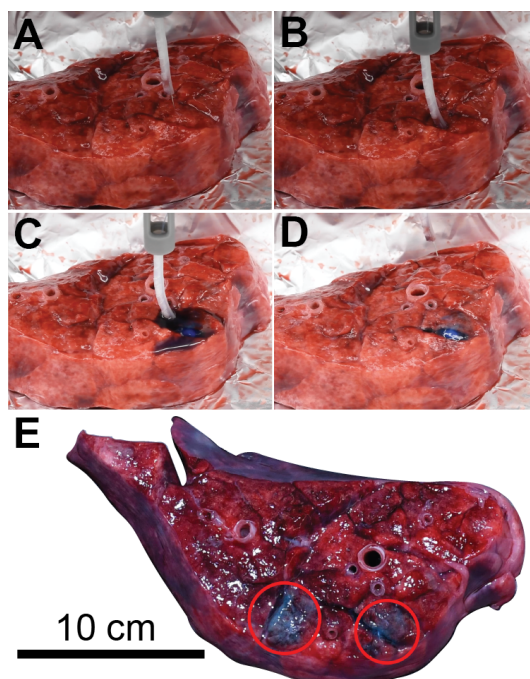


Figure 6: *Ex-vivo* test showing the soft robot capability to perform tissue puncturing and injection of dyed water (drug model). Please see Movie S1 for a complete visualization of this test. A)-D) Test sequence. E) Detail of two different testing locations with dyed water in the lung after experiment.

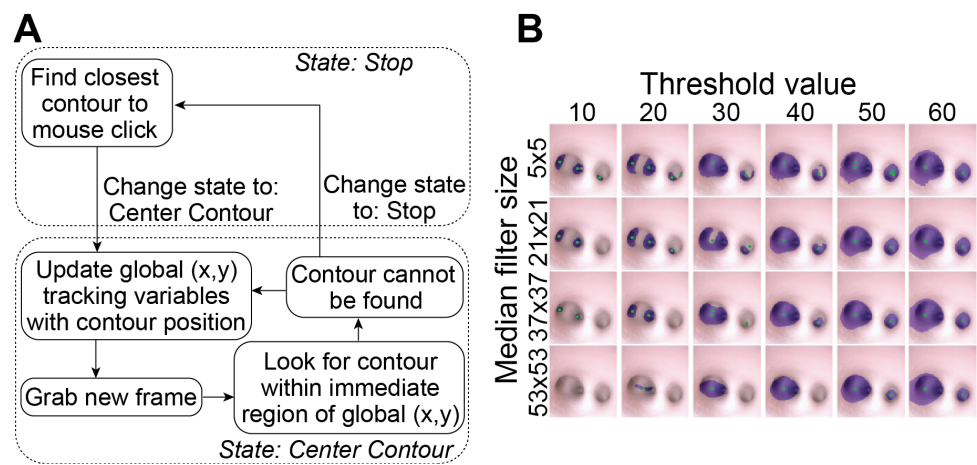


Figure 7: Contour tracking algorithm. A) An illustration of the logic used to achieve contour tracking. B) Results showing the contours with various combinations of threshold values and median filter sizes.

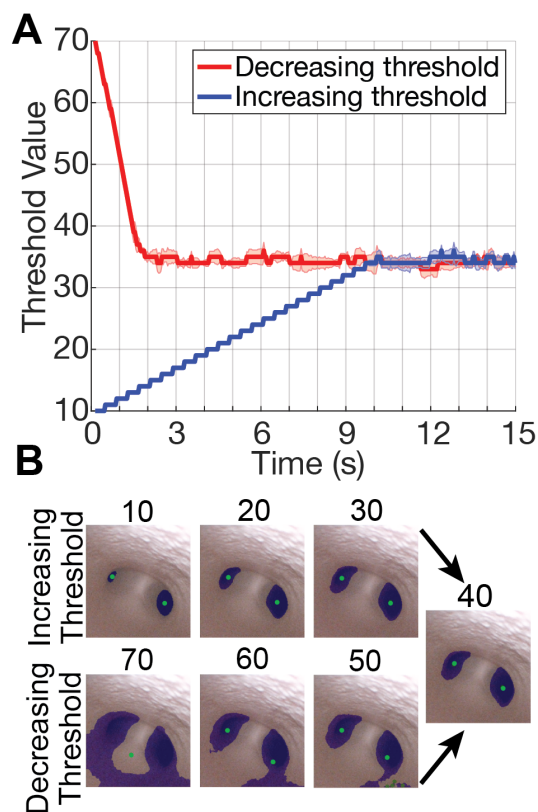


Figure 8: Adaptive threshold algorithm. A) Plot of threshold value versus time during dynamic thresholding. B) These images show the contours of the image that are found at the different threshold values as the image is stabilizing. The image under the column heading 40 is the final threshold value from the dynamic threshold operation.

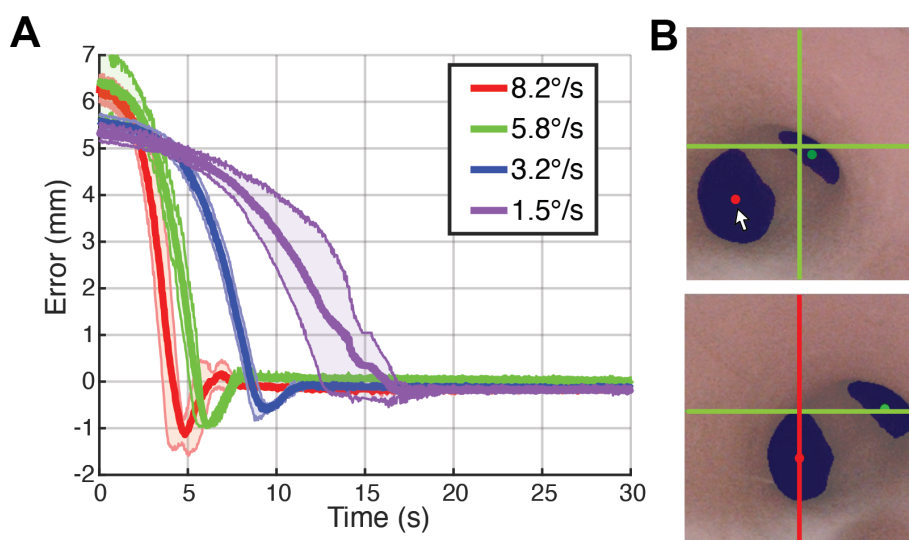


Figure 9: A) Plot of the position error versus time showing the alignment of the center of mass of a contour to the center of the vertical plane of the image. The trials were run with four different angular velocities of the robot. The solid line is the mean resulting from three experiments and the shaded area is the standard deviation. B) Graphic user interface that allows the clinician to select the branch to align to (top) and robot tip steering towards desired direction (bottom). Corresponding pressurization of the soft robot during this experiment are reported in Fig. S10.

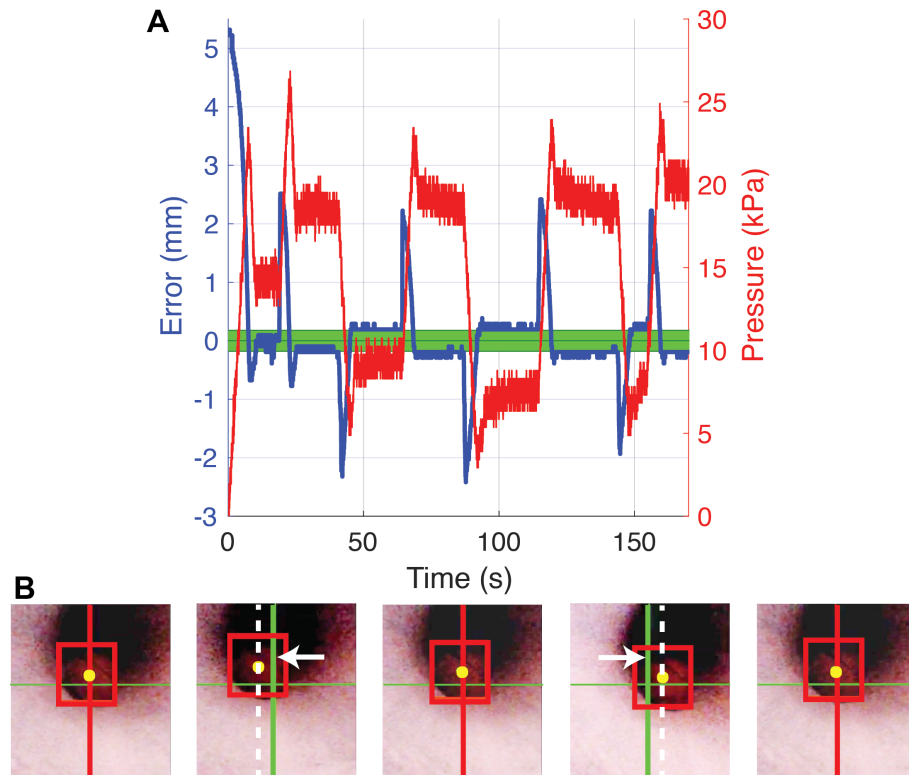


Figure 10: Template tracking algorithm. A) Plot showing the error between the position of the center of mass of the lesion and the center plane of the image and the pressure variation versus time. The green region shows 0.180 mm (0 ± 2 pixels) from the center of the vertical plane which is considered aligned. B) Automated tracking and aligning to a lesion: two perturbations are shown (in two different directions). From left to right: 1) the system is centered on the lesion, 2) it is perturbed and moved towards the right, 3) it recovers its position in front of the lesion, 4) it is perturbed again and moved towards the left, 5) it recovers its position again.